A&A 367, 959–966 (2001)
DOI: 10.1051/0004-6361:20000415

Astronomy
&
Astrophysics

A precessing, variable velocity jet model for DG Tauri

A. Raga[1,2], S. Cabrit[2], C. Dougados[3,4], and C. Lavalley[3]

[1] Instituto de Astronomía, UNAM, Apartado Postal 70-264, 04510 D. F., Mexico
[2] Observatoire de Paris, DEMIRM, UMR 8540 du CNRS, 61 avenue de l'Observatoire, 75014 Paris, France
[3] Laboratoire d'Astrophysique, Observatoire de Grenoble, CNRS/UJF UMR 5571, BP 53,
38041 Grenoble Cedex 9, France
[4] Canada-France-Hawaii Telescope Corporation, PO Box 1597, Kamuela HI 96743, USA

Received 1 September 2000 / Accepted 30 November 2000

Abstract. We present a first attempt at reproducing the morphology and kinematical properties of the DG Tau microjet using a 3D hydrodynamical numerical simulation of a precessing, variable velocity jet. Synthetic maps and position-velocity diagrams in Hα and [O I]λ6300 are calculated and compared with recent imaging and spectro-imaging observations (Lavalley-Fouquet et al. 2000; Dougados et al. 2000). Several observed properties are qualitatively reproduced, such as the knot separation, width, and asymmetric morphology, and the increase in ionization fraction and decrease in electronic density away from the star. However, the predicted kinematics in the region between the two jet knots differs from the observed behaviour. This discrepancy probably results from our simple assumption of a sinusoidal velocity variability, and points to a more complex velocity time-variability in the jet from DG Tau.

Key words. hydrodynamics – stars: individual: DG Tau – ISM: HH objects – ISM: individual objects: HH 158 – ISM: jets and outflows

1. Introduction

Even though most systems of Herbig-Haro (HH) objects are ejected by optically invisible, deeply embedded infrared or radio sources, some HH objects have a visible, T Tauri star as their source (see, e.g., Mundt & Fried 1983; and the catalogue of Reipurth 1999). Several T Tauri stars also show a collimated emission-line region extending away from the star for a few seconds of arc. These so-called "microjets" are identified through long-slit spectroscopy (Solf 1989, 1997; Hirth et al. 1994, 1997), and are believed to be the base of the HH flows sometimes observed at larger distances from the star. Thus, microjets allow us to probe the jet structure on smaller physical sizes ($\simeq 10^{16}$ cm at the distance of the Taurus cloud) and shorter time scales (a few years) than in usual HH flows.

The best studied microjet so far is the one from DG Tau. Discovered by Mundt & Fried (1983), it was then studied through long-slit spectroscopy (Mundt et al. 1987; Solf & Böhm 1993; Solf 1997) and imaged with the Hubble Space Telescope (Kepner et al. 1993; Stapelfeldt et al. 1997). Detailed spectro-imaging studies of the two-dimensional jet structure on sub-arcsecond scales were presented by Lavalley et al. (1997), Lavalley-Fouquet et al. (2000), and Bacciotti et al. (2000). These studies reveal several interesting properties including: (1) the presence of two knots at 1″ and 3.″6 from the star with morphology and kinematics suggestive of bow shocks created by jet variability; (2) a line excitation apparently dominated by shocks, with ionization fraction increasing away from the star (Lavalley-Fouquet et al. 2000); (3) a larger jet width at lower radial velocities, with indications of a very low-velocity halo surrounding the jet in [O I]; (4) wiggles in the jet beam.

The latter property of the DG Tau microjet is especially striking in 0.″1 resolution adaptive-optics images recently obtained by Dougados et al. (2000). The [O I] image shows that the microjet ejected by DG Tauri has a curved structure, which enters a bow-shaped knot along the northern bow wing. This kind of structure (in which a jet enters a bow-shaped knot along one of the bow wings) is also observed in other HH jets. For example, in HH 46/47 the jet enters the 47A condensation along its western edge. Even though the spatial scale of this HH flow is approximately one order of magnitude larger than the one of the DG Tauri microjet, the morphological similarity between the two objects is remarkable (see Heathcote et al. 1996; Dougados et al. 2000). Interestingly, the two other microjets imaged by Dougados et al. (2000), driven by CW Tau and RW Aur, are very straight and much

---

Send offprint requests to: A. Raga,
e-mail: `raga@astroscu.unam.mx`

narrower than the DG Tau microjet. It is tempting to speculate that precession of the jet axis might be responsible for both the observed curvature and the larger width of the DG Tau jet, compared to these other two microjets.

In this paper, we present a first attempt at reproducing the morphology and kinematics of the DG Tau microjet by a time-variable jet, using a 3D gasdynamic numerical simulation. We do not include a magnetic field in this simulation, as there are no direct measurements of the magnetic field strengths in HH jets (see, e.g., Hartigan et al. 1994), and there also is no clear theoretical consensus about the geometry and strength of the magnetic field in these objects. In the simulation, we introduce a sinusoidal variability of the ejection velocity, in order to form knots with the appropriate separations. We also introduce a precession of the outflow axis, to produce the observed curvature of the jet beam.

The precession results in off-centre positions for the jet beam as it enters the successive working surfaces of the flow, and broadens the working surface to a diameter comparable to the local width of the precession cone. This effect has been studied before in the context of extragalactic jets, having received the uncomfortable name of "dentist's drill model" (Cox et al. 1991). Even though there are a number of papers about HH jets with variable ejection directions (Raga et al. 1993; de Gouveia dal Pino et al. 1995; Cliffe et al. 1996; Suttner et al. 1997), none of them have discussed the "dentist's drill" effect (with the exception of the discussion of 2D simulations of Biro et al. 1995), which has remained in the (almost) exclusive realm of extragalactic jets.

We first derive the parameters adopted for modeling the DG Tauri microjet (Sect. 2), and then discuss a 3D numerical simulation carried out with these parameters (Sect. 3). Predicted intensity maps and position-velocity diagrams are presented in Sect. 4. Finally, we discuss the relative success of the model at explaining the observational characteristics of DG Tauri, in particular the velocity gradients along and perpendicular to the jet axis (Sect. 5).

From the numerical point of view, this work is similar to the one of Raga et al. (2001), who presented a variable ejection jet model for the "triple source" radio continuum jet in Serpens (see, e.g., Curiel et al. 1993). The comparison between the model and the DG Tauri microjet presented in this paper is a natural step forward from the previous work in that it involves a comparison of predicted and observed emission line fluxes and line profiles, while the previous work was restricted to a comparison of only the predicted and observed radio continuum fluxes.

2. Parameters for the DG Tauri microjet

In a series of papers, we have presented spectro-imaging observations obtained with the TIGRE and OASIS integral field spectrographs at the Canada-France-Hawaii Telescope (Lavalley et al. 1997; Lavalley-Fouquet et al. 2000) and adaptive optics narrow-band images, also obtained at the same telescope (Dougados et al. 2000) in the Hα, [O I] 6300, [N II] 6583 and [S II] 6717, 31 lines. These data provide extensive information about the physical conditions, radial velocities and proper motions of the DG Tauri microjet, which we use to choose the parameters for a gasdynamic numerical simulation.

We adopt a distance of 140 pc to the Taurus star formation region, and we consider that the jet is pointing towards the observer at a $\phi = 48°$ angle with respect to the plane of the sky (following Lavalley-Fouquet et al. 2000, who determined this angle from radial velocity and proper motion measurements).

In order to deduce the parameters for a proposed ejection velocity variability, we use the following arguments.

In 97/01 and 98/01, the DG Tauri microjet showed two main knots with a projected separation of $\approx 2\farcs7$ (see Fig. 1 of Dougados et al. 2000 and Fig. 1 of Lavalley-Fouquet et al. 2000). The leading, bow-shaped knot of the microjet has a proper motion velocity of ≈ 200 km s^{-1} (cf. Fig. 4 of Dougados et al. 2000), which when corrected for projection effects gives a 300 km s^{-1} velocity for the material in the working surface. This working surface velocity should have a value close to the mean velocity v_0 of the time-dependent ejection velocity (see Kofman & Raga 1992), so that we obtain a $v_0 = 300$ km s^{-1} estimate for the mean velocity. From this value for v_0 and the knot separation (8.5 10^{15} cm after correction for projection effects) one obtains a $\tau_{\rm v} \simeq$ 9 yr timescale.

Another estimate of v_0 and $\tau_{\rm v}$ can be obtained from the average of the radial velocities immediately upstream and downstream of the main bow shock, $\simeq -350$ and -180 km s^{-1}, respectively (see Fig. 2 of Lavalley-Fouquet et al. 2000; and Fig. 7 of the present paper). After correction for projection, one finds $v_0 = 360$ km s^{-1} and $\tau_{\rm v} = 7.5$ yr. We thus adopt $v_0 = 300$ km s^{-1} and $\tau_{\rm v} = 8$ yr for our model.

We should note that the leading, bow-shaped knot of the DG Tau microjet clearly does not correspond to the leading knot of this outflow, as at least three more knots are detected at larger distances from the source. Using the proper motions and radial velocities of these knots measured by Eislöffel & Mundt (1998) and the separations between the successive knots, one obtains estimates for a variability timescale of $\sim$10 yr, which are consistent with the value of $\tau_{\rm v}$ which we have adopted.

Finally, fits to the observed line ratios in the two bright knots of the DG Tauri microjet suggest shock velocities of $\sim$70–100 km s^{-1} (Lavalley-Fouquet et al. 2000) which also agree with the radial velocity jump observed across the main bow shock. We therefore choose a $\Delta v = 100$ km s^{-1} half-amplitude for the ejection velocity variability.

We then carry out a numerical simulation in which the modulus of the ejection velocity v_j varies with time following

$$v_j(t) = v_0 + \Delta v \sin\left(\frac{2\pi t}{\tau_{\rm v}}\right) , \tag{1}$$

with the values of v_0, Δv and $\tau_{\rm v}$ derived above.

Also, the beam of the DG Tauri microjet describes a curved path in the plane of the sky, and enters the bow shock along one of the bow shock wings (see Dougados et al. 2000). In order to reproduce this kind of structure in our numerical simulation, we introduce a precession of the jet beam. It is difficult to estimate the parameters of this precession from the observations, but through a number of numerical simulations we have determined that a precession cone of half-opening angle $\theta_0 = 5°$ and precession period $\tau_\mathrm{p} = 8$ yr produces results which are compatible with the curved beam structure and wiggling observed in the DG Tauri microjet (Dougados et al. 2000; Lavalley-Fouquet et al. 2000).

We assume that the jet has a top-hat initial cross section, with a radius $r_\mathrm{j} = 3\ 10^{14}$ cm (corresponding to half of the $FWHM \simeq 0.25''$ measured at the base of the DG Tau jet by Dougados et al. 2000). We choose a $n_\mathrm{j} = 10^4$ cm initial density, which is a factor of a hundred lower than the initial density determined by Lavalley-Fouquet et al. (2000), but which is necessary in order not to have highly unresolved cooling regions behind the shocks in the flow.

As an example, we note that the cooling distance behind the bow shock of the knot located $z = 7\ 10^{15}$ cm from the source in Fig. 4 has a value of ≈1.5 10^{14} cm (which is the cooling distance to 10^4 K of a plane-parallel shock of velocity 100 km s^{-1} and pre-shock density 100 cm^{-3}, according to the tabulation of Hartigan et al. 1987). This cooling distance is only slightly larger than the resolution of our numerical sumulations (see the following section). However, there is of course a wide range of different cooling distances in the many shocks which appear in our simulations.

Finally, we assume that the surrounding environment is homogeneous, with a $n_\mathrm{env} = 1000$ cm^{-3} density. Both the environment and the jet are assumed to be initially neutral, and with a 10^3 K temperature.

3. The numerical model

We compute a 3D gasdynamic jet simulation with the parameters derived in Sect. 2 using the "yguazú-a" adaptive grid code. The details of this code are discussed by Raga et al. (2000). For the present application we use the version of the code described by Raga et al. (2001), who modeled the radio continuum emission from a jet with a variable ejection direction+velocity. In this version of the code, the 3D gasdynamic equations are integrated together with an equation for the ionization of hydrogen. Using the computed temperature, electron density and neutral fraction, a time-dependent cooling function is calculated (with the contribution from atoms other than hydrogen parametrized as described by Raga et al. 1999), and included in the energy equation.

The 3D numerical simulation is done on a 5-level, binary adaptive grid with a maximum resolution (in the three dimensions) of 1.17 10^{14} cm. This maximum resolution is only allowed in the region occupied by jet material, and the shortest grid spacing allowed for the environment is a factor of two higher than this value. The full computational domain is 7.5 10^{15} cm by 7.5 10^{15} cm by 1.5 10^{16} cm along $x-y-z$. The jet is injected at the origin of the coordinate system, with the axis of the precession cone being parallel to the z-direction, and the initial direction of the jet lying on the xz-plane, pointing towards the $+x$-direction (with the ejection direction starting to rotate towards the $+y$-direction). The parameters of the flow and the time-dependent ejection velocity are discussed in Sect. 2.

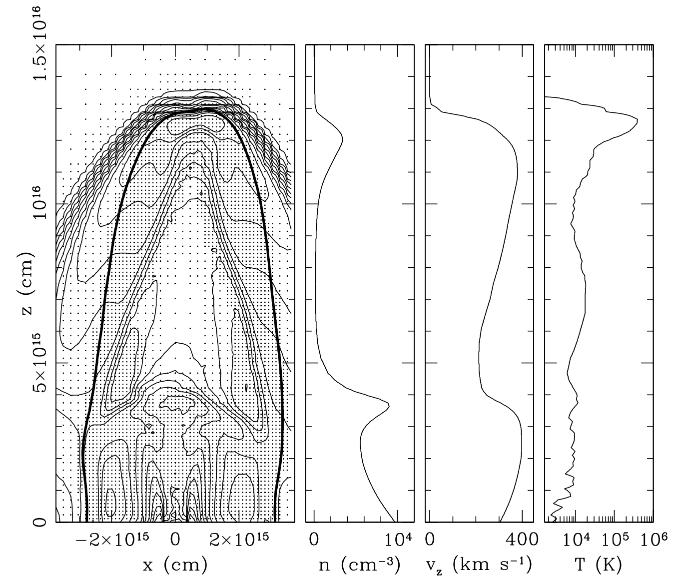

Fig. 1. Stratification of the jet flow obtained for a $t = 12$ yr time integration. The left frame shows the pressure stratification (factor of two contours), the contact discontinuity separating the jet and the environmental material (thick contour), and the grid points chosen by the adaptive grid algorithm on the xz-plane. The other three frames show cuts along the z-axis of number density (of atoms and ions), z-velocity and temperature of the flow

The flow stratification resulting from this simulation for a $t = 12$ yr time-integration is shown in Fig. 1. This figure shows the pressure stratification (on the xz-plane) and density, z-velocity and temperature as a function of position along the z-axis (at $x = 0$). At this time we see that the leading working surface is getting to the edge of the computational domain, and that a second working surface has already formed.

Even though the flow has a jet-to-environment density ratio of 10 and is highly radiative, a cocoon of jet material fills an approximate cylindrical region of ∼10 times the initial jet radius (see Fig. 1). This is an interesting characteristic of the flow, resulting from both the precession and the velocity time-variability. This cocoon shows an inner conical shock structure, which corresponds to a "tail shock" that trails the leading working surface.

From this numerical simulation, we have carried out predictions of emission maps and position-velocity diagrams, which we discuss in the following section.

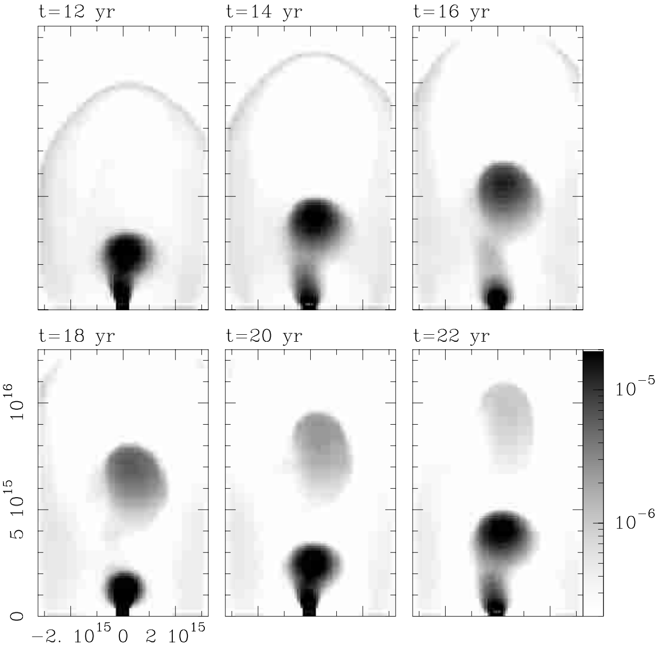

Fig. 2. [O I] 6300 intensity maps predicted from the numerical simulation for $t = 12$, 14, 16, 18, 20 and 22 yr integration times. A $\phi = 48^\circ$ angle has been assumed between the z-axis and the plane of the sky, as appropriate for the DG Tauri microjet (see Sect. 2). The logarithmic greyscale is in units of erg s^{-1} cm^{-2} sr^{-1}. The axes are labeled in cm

4. Predicted intensity maps and position-velocity diagrams

From the numerical simulation described in Sects. 2 and 3, we compute Hα and [O I] 6300 intensity maps and position-velocity diagrams. For each time frame, our gasdynamic code gives the temperature, density and hydrogen ionization fraction for all grid points. With this data, and assuming that the neutral fraction of oxygen follows the hydrogen neutral fraction (due to the high charge exchange rate between these two species), we can compute the Hα (considering both the effective recombination rate and the contribution due to collisional excitations from the ground state) and the [O I] 6300 emission coefficients (using the parameters of Mendoza 1983, with a linear fit to the temperature dependence of collision strengths). We have assumed an abundance of 6.6 10^{-4} for oxygen (relative to hydrogen, by number), and a 3 10^{-4} abundance for carbon (which is considered only as a source of free electrons for the regions with neutral hydrogen). Once the emission coefficients have been computed, we can obtain predictions of intensity maps and position-velocity diagrams by carrying out the appropriate line-of-sight integrations.

Figure 2 shows the [O I] 6300 intensity maps predicted for several different integration times, assuming a $\phi = 48^\circ$ angle between the z-axis and the plane of the sky, as appropriate for the DG Tauri microjet (see Sect. 2). The corresponding [O I] 6300 position-velocity diagrams are shown in Fig. 3. The line profiles were computed for a spectrograph slit of 2″ width (corresponding to ≈4 10^{15} cm at the distance of DG Tauri) straddling the projection of the z-axis on the plane of the sky.

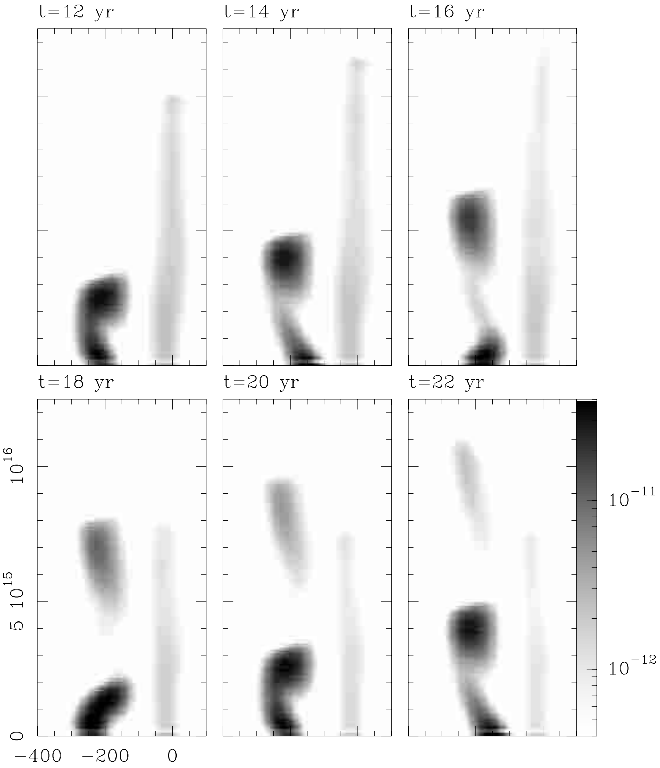

Fig. 3. [O I]6300 position-velocity diagrams predicted from the numerical simulation for $t = 12$, 14, 16, 18, 20 and 22 yr integration times. A $\phi = 48^\circ$ angle has been assumed between the z-axis and the plane of the sky (pointing towards the observer), as appropriate for the DG Tauri microjet (see Sect. 2). The line profiles have been computed assuming that the spectrograph slit straddles the z-axis, and has a width of 2″ (corresponding to ≈4 10^{15} cm at the distance of DG Tauri). The results have been convolved with a $FWHM = 50$ $\mathrm{km\,s^{-1}}$ Gaussian "instrumental profile". The logarithmic greyscale is in units of erg s^{-1} cm^{-1} sr^{-1} $(\mathrm{cm/s})^{-1}$. The position (vertical) axis is labeled in cm, and the radial velocity axis in $\mathrm{km\,s^{-1}}$

In Fig. 2, we see the leading working surface, which already starts to leave the computational grid at $t = 16$ yr. The emission from the bow shock of this working surface is very weak because the shock is non-radiative (as it has a cooling distance of the order of ten times the jet radius, and a cooling timescale of 22 years, as can be seen from the 300 $\mathrm{km\,s^{-1}}$ shock velocity model of Hartigan et al. 1987). The second working surface monotonically becomes fainter with increasing time starting from the $t = 12$ yr map (Fig. 2). The third working surface is clearly visible in the $t = 18$ yr map, showing a time evolution which is most similar to the one of the second working surface (as can be seen by comparing the $t = 20$ with the $t = 12$ yr maps, or the $t = 22$ with the $t = 14$ yr maps).

In the intensity maps, we also see the effects of the precession of the jet beam. As the precession and velocity variability have $\tau_{\mathrm{p}} = \tau_{\mathrm{v}} = 8$ yr (see Sect. 2), the two variabilities are synchronized. At the time one of the

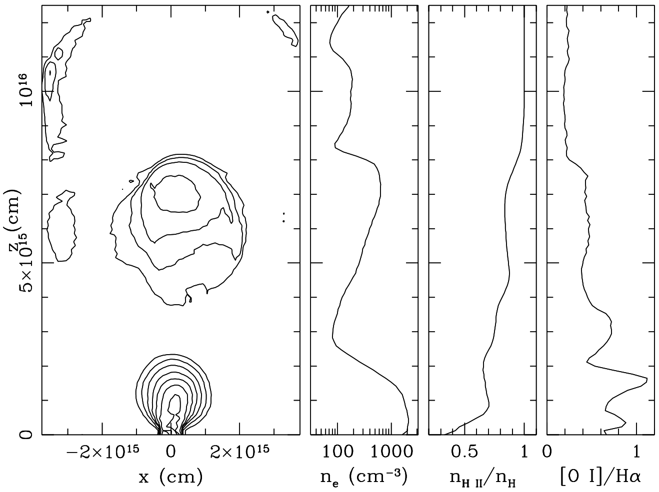

Fig. 4. Results from the model for a $t = 18$ yr time integration. The graph shows the Hα intensity map (left, factor of 2 contours), the average electron density, the average hydrogen ionization fraction and the [O I] 6300/Hα line ratio (right) as a function of position along the projected direction of the precession cone, assuming a $\phi = 48°$ angle between the z-axis and the plane of the sky

working surfaces is starting to appear (see, e.g., the $t = 16$ and 18 yr intensity maps of Fig. 2), the ejection direction approximately lies on the xz-plane, pointing towards the $+x$-direction.

The jet beam joining the source and the working surface, however, is formed by material ejected in between the times when the working surfaces appear, when the ejection direction points mostly in the $-x$-direction. This results in the formation of working surfaces with an extension in the $+x$-direction, which have the jet beam entering them along the $-x$-directed bow wing (see, e.g., the $t = 14$ and 16 yr maps of Fig. 2). This is an example of the so-called "dentist's drill" effect, which results in a relatively wide working surface being formed by a much thinner jet (see Cox et al. 1991).

In order to have predictions that can be compared with the spectroscopic data of Lavalley-Fouquet et al. (2000) and the HST STIS spectra of Bacciotti et al. (2000), the position-velocity diagrams of Fig. 3 have been convolved with a $FWHM = 50\ \mathrm{km\,s^{-1}}$ Gaussian "instrumental profile". These diagrams show the "saw tooth" signature expected for jets with a variable ejection velocity (see, e.g., Raga et al. 1990). As the precession cone has a small ($\theta_\mathrm{p} = 5°$, see Sect. 2) opening angle, no clear effects of the precession are seen in the position-velocity diagrams. An interesting result is that we see a slow component of the emission line profiles (at radial velocities between 0 and -50 km s^{-1} in all time frames) which comes from the cocoon of warm jet and environmental gas which surrounds the jet beam.

Finally, in Fig. 4 we show the Hα intensity map predicted for $t = 18$ yr, together with the electron density, hydrogen ionization fraction and [O I] 6300/Hα line ratio averaged across the width of the spectrograph slit (which straddles the z-axis and has a projected width of 2 10^{15} cm, as described above). The electron density and hydrogen ionization fractions have been calculated by carrying out averages along lines of sight, weighted by the $n_\mathrm{e}\,n_\mathrm{H\,I}$ product (where n_e is the electron density, and $n_\mathrm{H\,I}$ is the neutral hydrogen density). These values therefore correspond in an approximate way to the values that would be obtained from analyses of line ratios involving low ionization species (see Bacciotti & Eislöffel 1999; Lavalley-Fouquet et al. 2000), which have emission coefficients which approximately scale as $n_\mathrm{e}\,n_\mathrm{H\,I}$ (these emission coefficients, however, also have explicit dependencies on temperature).

5. A comparison with observations of the DG Tauri jet

The numerical simulation reproduces qualitatively well several characteristics of the DG Tauri microjet. For example, the [O I] 6300 PUEO image of the DG Tauri microjet (Dougados et al. 2000) has a morphology that resembles the ones obtained from the numerical model for $t = 16$ or 18 yr integration times (Fig. 2). The observed and predicted maps have main bow shocks with similar widths (and at similar distances from the source), show a knot that is beginning to emerge from the source region, and have a jet beam that enters the main bow shock along one of its wings. Furthermore, Fig. 4 shows that the simulation also reproduces well the increase in ionization fraction away from the star, and the accompanying factor of ∼10 decrease in electronic density, derived for the DG Tau microjet by Lavalley-Fouquet et al. (2000) through an analysis of forbidden emission line ratios. The predicted [O I]/Hα ratio lies in the same range as in the observations.

A comparison of the observed and predicted position-velocity diagrams perpendicular to the jet axis, presented in Fig. 5, also reveals interesting qualitative similarities. At all distances, there is a clear trend both in the observed and predicted diagrams that the transverse spatial extent of the emitting region is larger at lower radial velocities. Such a behaviour has been observed in knots ranging in distance from $1''$ to $10''$ along the DG Tau jet (Bacciotti et al. 2000; Lavalley et al. 1997; Mundt et al. 1987). In the simulation, this property arises from the presence of bow shock wings trailing behind each internal working surface, which produce laterally extended emission of lower radial velocities than the jet beam, down to $\simeq -100\ \mathrm{km\,s^{-1}}$. The magnitude of this effect is particularly well reproduced for the main bow shock structure at $3.6'' \simeq 7\ 10^{15}$ cm. Hence, we are able to produce the large width observed at that position even with an intrinsically narrow jet. A detailed comparison with the innermost part of the DG Tau jet is more difficult given the very complex kinematics in this region (which include a broad range of velocities not well reproduced by our simulation, see below).

The increase in jet width caused by the precession can be judged by comparing Fig. 5 with similar diagrams for

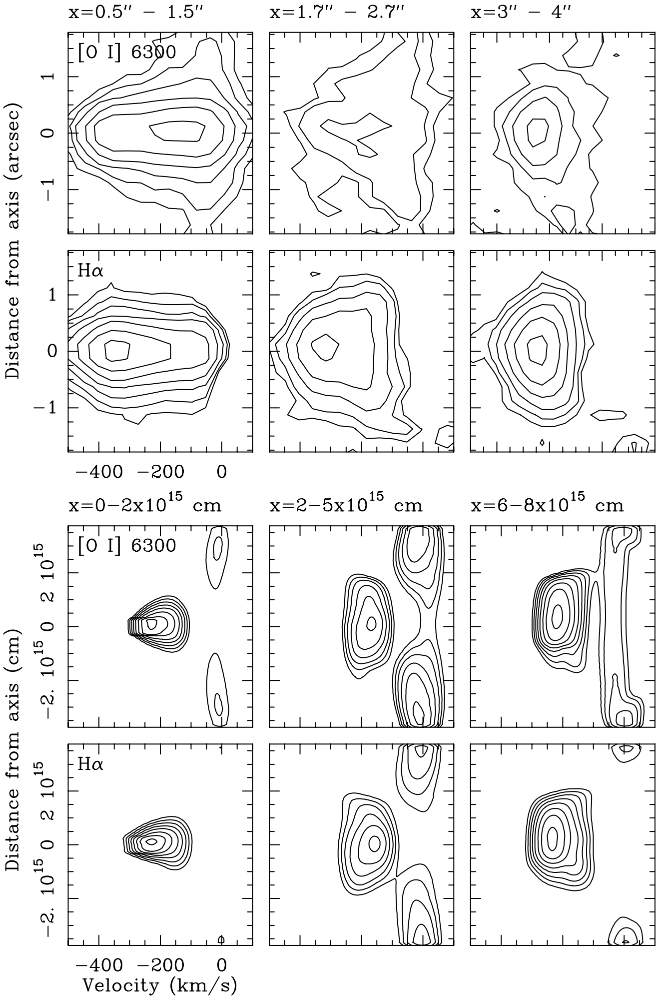

Fig. 5. PV diagrams perpendicular to the jet in [O I] and Hα, obtained at three different projected distances from the star (the range in x is indicated above each diagram). Top panels: observed diagrams derived from the OASIS spectro-imaging observations of Lavalley-Fouquet et al. (2000). Bottom panels: computed diagrams from the simulation at $t = 18$ yr, assuming a $\phi = 48°$ angle between the z-axis and the plane of the sky

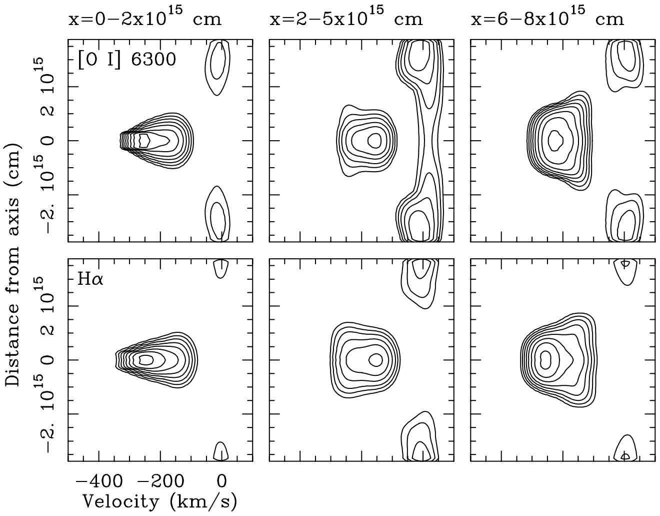

Fig. 6. PV diagrams perpendicular to the jet in [O I] and Hα, for the non-precessing jet simulation at $t = 18$ yr, at three different projected distances from the star (the range in x is indicated above each diagram), assuming a $\phi = 48°$ angle between the z-axis and the plane of the sky

a non-precessing jet simulation, with otherwise identical parameters, shown in Fig. 6. The effect is most apparent in the faint jet section between the two internal working surfaces, and also in the high-velocity apex of the working surface at 7 10^{15} cm from the source. A stronger broadening would be obtained for larger opening angles of the precession cone (for the model shown in Fig. 5, we have used a half-opening angle $\theta_0 = 5°$, see Sect. 2). This broadening of the working surfaces, together with the entrance of the jet beam along one of the bow shock wings (see Fig. 2) is what has been called the "dentist's drill" effect in the extragalactic jet literature (see Sect. 1 and Cox et al. 1991).

Another nice feature of the simulation is that the warm jet cocoon left behind by the leading working surface produces a low velocity emission component (radial velocity < -100 km s^{-1}), most apparent in [O I], which is very extended laterally. A low-velocity [O I] "halo" component of similar velocity and extent is indeed observed (Lavalley et al. 1997; Lavalley-Fouquet et al. 2000) and might be explained by such a jet cocoon. This halo is very weak in both the observed and predicted Hα position-velocity maps.

Interestingly, a comparison of the observed and predicted position-velocity diagrams *parallel* to the jet axis is less successful. In Fig. 7, we show the [O I] 6300 and Hα position-velocity diagrams obtained in 98/01 for the DG Tau microjet (Lavalley-Fouquet et al. 2000), as well as the corresponding predictions obtained from the numerical model for a $t = 18$ yr time integration (cf. Fig. 3). From this figure, it is clear that the observed and predicted kinematics are quite different from each other, except toward the main bow shock located at $z \simeq 7\ 10^{15}$ cm.

For example, the region within $\sim 0\farcs5$ from DG Tauri shows an "acceleration", with the mean velocity of the line profile becoming more negative away from the star. This effect is not seen in the numerical simulation, which shows a decreasing radial velocity modulus for increasing distances from the source. This steep velocity decrease, resulting from the fast jet catching up with previous slower ejecta, is actually responsible for the formation of the new knot at $\simeq 10^{15}$ cm from the star.

At distances $\geq 3\ 10^{15}$ cm ($1\farcs5$) from the source, the predicted position-velocity diagram does show an increasing velocity vs. position, from $\simeq -150$ km s^{-1} up to the bow shock velocity. A comparable increase is indeed observed in the [O I] line profiles of the DG Tauri microjet (see Fig. 7). However, observed line profiles in this region also exhibit, especially in Hα, a high-velocity component at an almost constant radial velocity of ≈ -300 km s^{-1} which is not reproduced by our simulation.

We have tried to run other numerical simulations with sinusoidal, time-dependent ejection velocities, but we

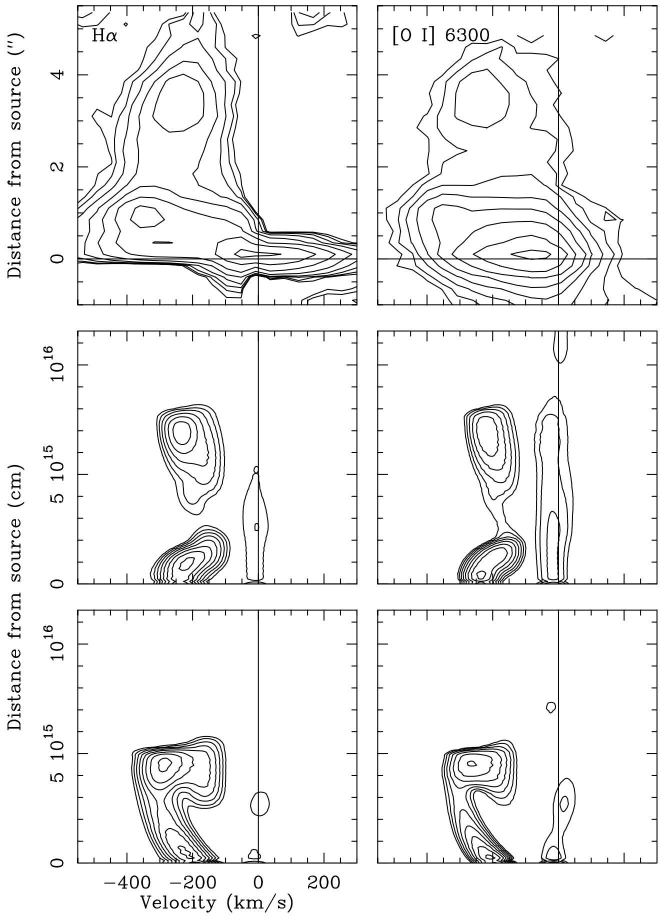

Fig. 7. PV diagrams parallel to the jet in [O I] and Hα. Top panels: observed diagrams derived from the OASIS spectro-imaging observations of Lavalley-Fouquet et al. (2000). Middle panels: computed diagrams from the simulation at $t = 18$ yr (cf. Fig. 3), assuming a $\phi = 48^\circ$ angle between the z-axis and the plane of the sky. Bottom panels: computed diagrams for a simulation with an alternative set of parameters (see text)

have been unable to find a set of parameters that better reproduces the observed position-velocity diagrams. An example of the results obtained for an alternative set of parameters is shown in the bottom frames of Fig. 7 (corresponding to a $t = 16$ yr time-integration of a model with $v_0 = 350$ km s^{-1}, $\Delta v = 150$ km s^{-1}, $\tau_\mathrm{v} = \tau_\mathrm{p} = 10$ yr and with the other parameters identical to those discussed in Sect. 2). For this alternative model, we are showing a time-step where the next working surface has not yet formed. As a result, the radial velocity is steadily increasing all the way from the origin to the working surface, with the velocity just upstream of the main working surface being close to the maximum jet speed (a similar evolution stage is encountered at $t = 14$ yr for our first model; cf. Fig. 3). For these alternative parameters, the maximum radial velocity is $\simeq -350$ km s^{-1}, close to what is observed in DG Tau. However, the emission knot observed closer to the star is then left unexplained.

We conclude that a sinusoidal time-variable jet velocity seems to be unable to reproduce the kinematics of both emission knots in the DG Tau microjet, in particular the fact that the jet radial velocity appears almost constant between the two knots. Another type of variability (linear increase, saw-tooth) and/or the presence of several modes would be necessary to explain the observed radial velocity structure.

6. Conclusions

We have used various observations of the DG Tauri microjet in order to determine the parameters for a velocity variability and a precession of the ejection (as well as the initial radius and density of the jet). With these parameters, we have computed a 3D gasdynamic simulation, from which we carry out predictions of emission line maps and position-velocity diagrams. A comparison of these predictions with the observations shows interesting successes and failures of the model.

As expected, we can produce knots with appropriate morphologies as a result of the ejection velocity variability. Through the precession, we can produce knots that are much broader than the jet diameter (as a result of the "dentist's drill" effect), with the jet beam entering along one of the "wings" of the knot emission. This is in good qualitative agreement with the observations of the DG Tauri microjet. The observed increase in ionization fraction, and decrease in electronic density, away from the star is also qualitatively reproduced.

The position-velocity diagrams perpendicular to the jet axis also show interesting agreement with recent spectro-imaging observations of DG Tauri (Lavalley-Fouquet et al. 2000). In particular, the models produce both a fast component of low [O I] 6300/Hα ratio (tracing the jet beam and the internal working surfaces), and a much broader, low velocity component with a high [O I] 6300/Hα ratio (coming from the warm cocoon around the jet). This broader "wake" could possibly explain the low-velocity [O I] halo observed in DG Tau (Lavalley et al. 1997), although an explanation in terms of an intrinsic transverse jet structure is definitely not excluded by our observations.

The predicted radial velocity gradients along the jet axis, however, differ in an appreciable way from the observed behaviour. For example, in the region within $\sim 1''$ from the source, an "acceleration" (towards more negative velocities) is observed in the DG Tauri microjet. Our model does predict such "accelerations" (see, e.g., the $t = 14$ yr position-velocity diagram of Fig. 3), but occuring over considerably larger distances. Also, observations show a high-velocity component of almost constant radial velocity $\simeq -300$ km s^{-1} between the two working surfaces, while our model predicts a much lower velocity in this region once the second working surface has formed.

Such discrepancies with the observed velocity gradients can be attributed to the simplifying assumption in the present model that the ejection velocity variability is sinusoidal. A better agreement with the observations might be obtained by considering other types of velocity variabilities which could range from an asymmetric "rapid rise/slow decay" periodic variability to a more general, non-periodic ejection velocity history. This will require introducing more free parameters, for which additional observational constraints are needed.

Presently, there is no clear idea about the nature of the perturbations that could produce the ejection velocity time-variability necessary for reproducing the observed knot structure. The precession of the outflow axis necessary for modelling the structure of the jet could be the result of a precession of the accretion disk caused by the presence of a companion star, but in order to produce the ∼10 yr precession period (implied by the curved jet structure), a binary orbit with a very short period of ∼0.5 yr would be necessary (as the disk precession period is of ∼20 times the orbital period, according to Terquem et al. 1999; Bate 2000). Fortunately, the evolutionary timescales of the DG Tauri microjet are so rapid that we should have the exciting opportunity of discovering the precise nature of the variability of the ejection through direct observations and 3D hydrodynamic modelling of this object over the next two decades.

Acknowledgements. The work of AR was supported by the CONACyT grants 32753-E and 27546-E. AR also acknowledges support from a Fellowship of the John Simon Guggenheim Memorial Foundation, and the Observatoire de Paris for an Enseignant Invité position. We would like to thank Adam Frank (the referee) for helpful comments about this paper.

References

Bacciotti, F., & Eislöffel, J. 1999, A&A, 342, 717
Bacciotti, F., Mundt, R., Ray, T. P., et al. 2000, ApJ, 537, L49
Bate, M. R. 2000, MNRAS, 314, 33
Biro, S., Raga, A. C., & Cantó, J. 1995, MNRAS, 275, 557
Cliffe, J. A., Frank, A., & Jones, T. W. 1996, MNRAS, 282, 1114
Cox, C. I., Gull, S. F., & Scheuer, P. A. G. 1991, MNRAS, 252, 558
Curiel, S., Rodríguez, L. F., Moran, J. M., & Cantó, J. 1993, ApJ, 415, 191
de Gouveia dal Pino, E. M., Birkinshaw, M., & Benz, W. 1995, ApJ, 460, L111
Dougados, C., Cabrit, S., Lavalley, C., & Ménard, F. 2000, A&A, 357, 51
Eislöffel, J., & Mundt, R. 1998, AJ, 115, 1554
Hartigan, P., Raymond, J., & Hartmann, L. 1987, ApJ, 316, 323
Hartigan, P., Morse, J. A., & Raymond, J. 1994, ApJ, 436, 125
Hartigan, P., Edwards, S., & Gandhour, L. 1995, ApJ, 452, 736
Heathcote, S., Morse, J. A., Hartigan, P., et al. 1996, AJ, 112, 1141
Hirth, G. A., Mundt, R., & Solf, J. 1994, A&A, 285, 929
Hirth, G. A., Mundt, R., & Solf, J. 1997, A&AS, 126, 437
Kepner, J., Hartigan, P., Yang, C., & Strom, S. 1993, ApJ, 415, L119
Kofman, L., & Raga, A. C. 1992, ApJ, 390, 359
Lavalley, C., Cabrit, S., & Dougados, C. 1997, A&A, 327, 671
Lavalley-Fouquet, C., Cabrit, S., & Dougados, C. 2000, A&A, 356, L41
Mendoza, C. 1983, in Planetary Nebulae, IAU 103, ed. D. R. Flower (Dordrecht: Reidel), 143
Mundt, R., & Fried, J. W. 1983, ApJ, 274, L83
Mundt, R., Brugel, E. W., & Bührke, T. 1987, ApJ, 319, 275
Raga, A. C., Cantó, J., Binette, L., & Calvet, N. 1990, ApJ, 364, 601
Raga, A. C., Cantó, J., & Biro, S. 1993, MNRAS, 260, 163
Raga, A. C., Curiel, S., Rodríguez, L. F., & Cantó, J. 2001, A&A, in press
Raga, A. C., Mellema, G., Arthur, S. J., et al. 1999, RMxAA, 35, 123
Raga, A. C., Navarro-González, R., & Villagrán-Muniz, M. 2000, RMxAA, 36, 67
Reipurth, B. 1999, A Catalogue of Herbig-Haro Objects, published electronically (`http://casa.colorado.edu/`).
Solf, J. 1989, in ESO Workshop on Low Mass Star Formation and Pre-Main Sequence Objects, ed. B. Reipurth (Garching: ESO), 399
Solf, J., & Böhm, K. H. 1993, ApJ, 410, L31
Solf, J. 1997, in IAU Symposium No. 182: Herbig-Haro Flows and the Birth of Low Mass Stars, ed. B. Reipurth, & C. Bertout (Kluwer: Dordrecht), 63
Stapelfeldt, K., Burrows, C. J., & Krist, J. E. 1997, in Herbig-Haro Flows and the Birth of Low Mass Stars, IAU 182, ed. B. Reipurth, & C. Bertout (Kluwer: Dordrecht), 355
Suttner, G., Smith, M. D., Yorke, H. W., & Zinnecker, H. 1997, A&A, 318, 595
Terquem, C., Eislöffel, J., Papaloizou, J. C. B., & Nelson, R. P. 1999, ApJ, 512, L131